

In situ study of the formation mechanism of two-dimensional superlattices from PbSe nanocrystals

Geuchies, Jaco J.; Van Overbeek, Carlo; Evers, Wiel H.; Goris, Bart; De Backer, Annick; Gantapara, Anjan P.; Rabouw, Freddy T.; Hilhorst, Jan; Peters, Joep L.; Konovalov, Oleg

DOI

[10.1038/nmat4746](https://doi.org/10.1038/nmat4746)

Publication date

2016

Document Version

Accepted author manuscript

Published in

Nature Materials

Citation (APA)

Geuchies, J. J., Van Overbeek, C., Evers, W. H., Goris, B., De Backer, A., Gantapara, A. P., Rabouw, F. T., Hilhorst, J., Peters, J. L., Konovalov, O., Petukhov, A. V., Dijkstra, M., Siebbeles, L. D. A., Van Aert, S., Bals, S., & Vanmaekelbergh, D. (2016). In situ study of the formation mechanism of two-dimensional superlattices from PbSe nanocrystals. *Nature Materials*, *15*(12), 1248-1254. <https://doi.org/10.1038/nmat4746>

Important note

To cite this publication, please use the final published version (if applicable). Please check the document version above.

Copyright

Other than for strictly personal use, it is not permitted to download, forward or distribute the text or part of it, without the consent of the author(s) and/or copyright holder(s), unless the work is under an open content license such as Creative Commons.

Takedown policy

Please contact us and provide details if you believe this document breaches copyrights. We will remove access to the work immediately and investigate your claim.

1 In-situ study of the formation mechanism of two-dimensional superlattices from PbSe 2 nanocrystals

3 Jaco J. Geuchies^{1,5a†}, Carlo van Overbeek^{1†}, Wiel H. Evers^{2,3}, Bart Goris⁴, Annick de Backer⁴, Anjan P.
4 Gantapara⁶, Freddy. T. Rabouw¹, Jan Hilhorst^{5b}, Joep L. Peters¹, Oleg Konovalov^{5a}, Andrei V.
5 Petukhov^{7,8}, Marjolein Dijkstra⁶, Laurens D.A. Siebbeles², Sandra van Aert⁴, Sara Bals⁴ and Daniel
6 Vanmaekelbergh^{1*}

7
8 † These authors contributed equally to this work

9 *Corresponding author: Prof. dr. Daniel Vanmaekelbergh. Email: d.vanmaekelbergh@uu.nl

10

11 1 Condensed Matter and Interfaces, Debye Institute for Nanomaterials Science, Utrecht University,
12 The Netherlands

13 2. Optoelectronic Materials Section, Department of Chemical Engineering, Delft University of
14 Technology, The Netherlands

15 3. Kavli Institute of Nanoscience, Delft University of Technology, The Netherlands

16 4. Electron Microscopy for Materials Science (EMAT), University of Antwerp, Belgium

17 5. ^aID10/ ^bID01, European Synchrotron Radiation Facility (ESRF), France

18 6. Soft Condensed Matter, Debye Institute for Nanomaterials Science, Utrecht University, The
19 Netherlands

20 7. Physical and Colloidal Chemistry, Debye Institute for Nanomaterials Science, Utrecht University, The
21 Netherlands

22 8. Laboratory of Physical Chemistry, Department of Chemical Engineering and Chemistry, Eindhoven
23 University of Technology, The Netherlands

24

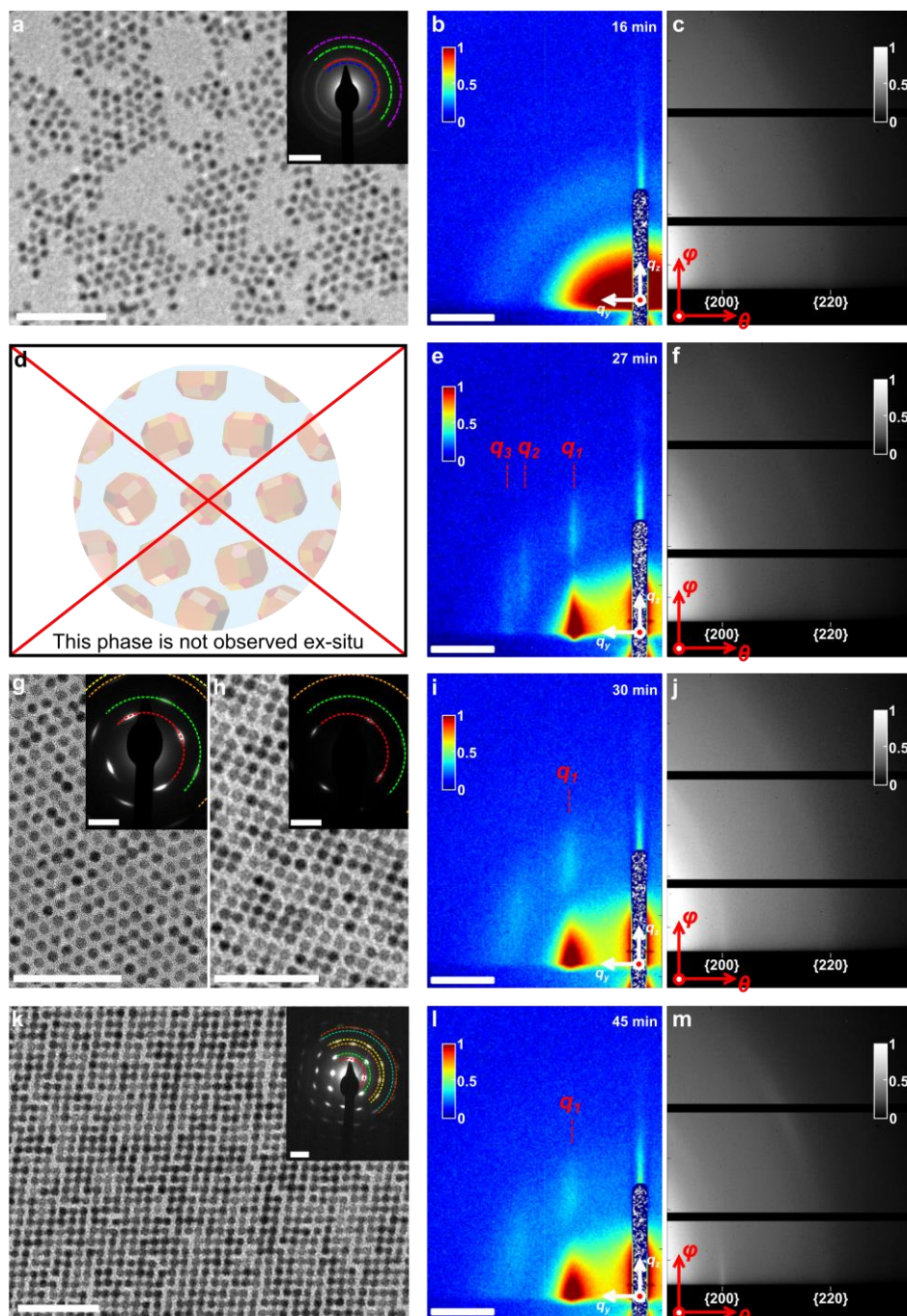
25 **Oriented attachment of PbSe nanocubes can result in the formation of two-dimensional (2-D)**
26 **superstructures with long-range nanoscale and atomic order [1,2]. This questions the applicability of**
27 **classic models in which the superlattice grows by first forming a nucleus, followed by sequential**
28 **irreversible attachment of nanocrystals [3,4], as one misaligned attachment would disrupt the 2D order**
29 **beyond repair. Here, we demonstrate the formation mechanism of 2-D PbSe superstructures with**
30 **square geometry by using in-situ grazing-incidence X-ray scattering (small-angle and wide-angle), ex-situ**
31 **electron microscopy, and Monte Carlo simulations. We observed nanocrystal adsorption at the**
32 **liquid/gas interface, followed by the formation of a hexagonal nanocrystal monolayer. The hexagonal**
33 **geometry transforms gradually through a pseudo-hexagonal phase into a phase with square order,**
34 **driven by attractive interactions between the {100} planes perpendicular to the liquid substrate, which**
35 **maximize facet-to-facet overlap. The nanocrystals then attach atomically via a necking process,**
36 **resulting in 2-D square superlattices.**

37 Oriented atomic attachment of colloidal nanocrystals (NCs), i.e. the formation of a single crystal by
38 atomic connection of smaller crystals, is an important process in geology [5-8], and recently gained
39 much attention as a preparation tool in semiconductor nanoscience [9,10]. We reported a method to
40 prepare 2-dimensional atomically coherent PbSe superlattices, starting from a suspension of PbSe
41 NCs [1,2]. The NCs have the shape of a truncated cube, consistent with the rock salt crystal structure
42 of PbSe (see Fig. S1). A suspension of these NCs is cast onto a surface of an immiscible liquid, ethylene
43 glycol, and the solvent is evaporated at room temperature. During the evaporation, extended sheets
44 are formed with a thickness of one NC monolayer [1].

45 The 2-D structure shows a nanoscale geometry with square periodicity with, to some extent, also
46 atomic coherency. In this so-called square geometry, all NCs are directed with a $\langle 100 \rangle$ axis
47 perpendicular to the 2-D plane, and are laterally connected via the in-plane $\{100\}$ facets. This means
48 that two out of six $\{100\}$ facets, namely those at the top and the bottom of the 2-D sheet, are not
49 used for attachment.

50 Nanocrystal self-assembly and atomic attachment forms a unique route to prepare 2-D
51 semiconductors with a superimposed geometry on the nanometer scale that influences the band
52 structure and can result in semiconductors with Dirac-type valence and conduction bands and high
53 charge carrier mobility [10-14]. Although superlattices with a square geometry are slightly disordered
54 on the atomic scale, they show amazing long-range ordering on the nano-scale. A better
55 understanding of the formation process is required for further progress in the synthesis of these
56 systems. The 2-D long-range ordering cannot be explained in terms of the classic nucleation and
57 growth model [3,4]. In this model the interactions between a crystal (nucleus) and building blocks are
58 supposed to be relatively weak, in the order of a few $k_B T$. As a result, the building blocks can bind
59 and unbind to an existing crystal, until the optimal binding geometry is found, resulting in ordering
60 over long distances. In the case of superlattice formation by oriented attachment of NCs this
61 mechanism cannot be operative, because per NC-NC connection, chemical bonds are formed
62 between tens of atoms on opposing crystal facets. The corresponding energy change is orders of
63 magnitude larger than the thermal energy, and oriented attachment should therefore be irreversible.
64 Thus "incorrect" irreversible attachments should lead to disruption of the long-range nanoscale order
65 in the superlattice.

66 Here, we present a real-time study of the growth of 2-D superlattices with a square periodicity. We
67 monitor the reactive self-assembly in real time and in-situ by simultaneous grazing-incidence small-
68 angle and wide-angle X-ray scattering (GISAXS and GIWAXS), see Fig. S1. Moreover, we scoop the
69 structures formed at different stages of the process for analysis with ex-situ Transmission Electron
70 Microscopy (TEM). Previous work on self-assembly of NCs has either focused on only monitoring the
71 long-range order on the NC scale using GISAXS [15], ex-situ measurements using GISAXS and GIWAXS
72 [16-19] and time resolved GISAXS and GIWAXS on the 3-D self-assembly of PbS nanocrystals, showing
73 an FCC-to-BCC phase transition [20]. We find that oriented attachment of the nanocrystals by neck
74 formation is preceded by a remarkable sequence of processes: nanocrystal adsorption at the
75 liquid/air interface with the preservation of the rotational degrees of freedom, formation of a dense
76 hexagonal NC phase, finally followed by a phase transition from hexagonal into square order in the NC
77 monolayer in which the rotations become entirely frozen.



78 **Figure 1: The different stages of the self-assembly process towards an oriented attached PbSe NC**
 79 **superlattice.** Ex-situ TEM images and in-situ X-ray scattering data are taken at different stages in the
 80 hexagonal-to-square phase transition. Top to bottom rows show the different phases over time. **(a)**
 81 TEM image of the disordered NCs, obtained by scooping immediately after drop casting on ethylene
 82 glycol. Inset shows the corresponding ED pattern, where diffraction rings indicate random orientations
 83 of the NCs, i.e. they have rotational freedom. **(b)** At the initial stage, we observe form factor scattering
 84 in GISAXS, indicating the presence of NCs without long-range positional order. **(c)** The GIWAXS pattern
 85 shows the full $\{200\}$ and $\{220\}$ diffraction rings of PbSe, indicating rotational freedom. **(d)** No
 86 hexagonal phase could be isolated ex-situ. **(e)** GISAXS pattern showing the presence of a hexagonal
 87 nanocrystal monolayer at the interface, with **(f)** the corresponding GIWAXS pattern. **(g)** TEM image of
 88 the pseudo-hexagonal phase, obtained when scooping the NCs just before toluene has completely
 89 evaporated. Inset: in ED the rings transformed into arcs. **(h)** TEM image of the initial square phase,
 90 before complete attachment of all NCs. Inset: the arcs in the ED have narrowed. **(i)** GISAXS pattern of

91 *the corresponding phase. Note that all peaks have broadened. (j) GIWAXS pattern corresponding to (i).*
92 *(k) TEM image of the final square phase. Inset: the ED pattern now consists of distinct spots, visible at*
93 *least up to the {600} reflection. (l) GISAXS pattern of the final square phase, with (m) the corresponding*
94 *GIWAXS pattern. Note how the diffraction rings have spots superimposed. The {200} diffraction has a*
95 *narrower width in the 2θ -direction than before (compare j), indicating that the NCs have attached in*
96 *this direction. All TEM scale bars correspond to 50 nm. The ED scale bars denote 20 nm^{-1} . The colored*
97 *rings in the ED patterns display the position of the diffraction rings: blue = {111}, red = {200}, green =*
98 *{220}, purple = {222}, orange = {400}, yellow = {420}, turquoise = {440}, brown = {600}. All GISAXS scale*
99 *bars denote 1 nm^{-1} .*

100 In Fig. 1 we follow the formation of the square superlattice starting from individual NCs, combining
101 ex-situ TEM and electron diffraction (ED) with in-situ GISAXS and GIWAXS. The TEM and X-ray
102 scattering measurements show the same stage in the NC assembly process. However, TEM data
103 should be interpreted with care as a structure extracted at a given time during the self-assembly
104 process may undergo changes during drying.

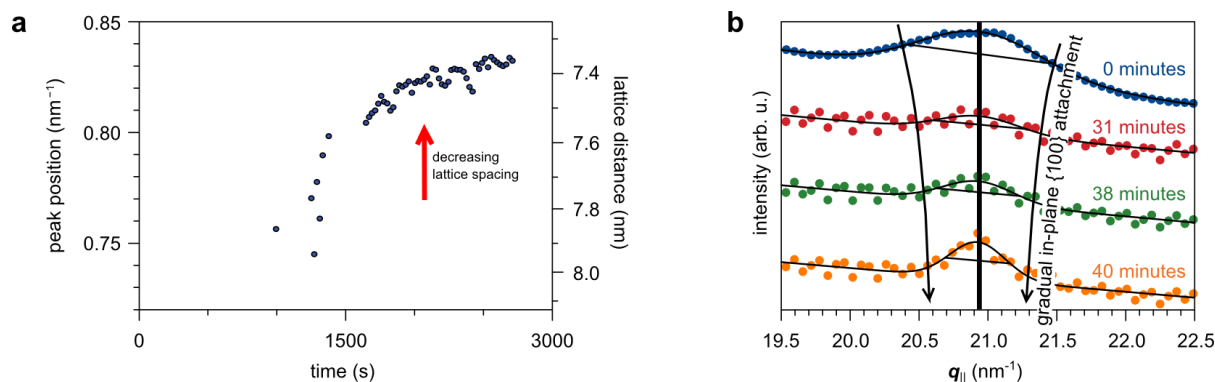
105 In the initial stages of the self-assembly process (16 minutes after the start of solvent evaporation), it
106 is not clear whether the NCs are still dispersed or already adsorbed at the toluene/air interface (Fig.
107 1(b,c)); but any long-range positional order (Fig. 1(a,b)) or atomic orientation (Fig. 1(c)) is lacking.

108 After 27 minutes, diffraction rods appear in the GISAXS pattern (Fig. 1(e)), at scattering vectors of 0.80
109 nm^{-1} , 1.39 nm^{-1} and 1.61 nm^{-1} , consistent with a 2-D hexagonal structure at the liquid-gas interface
110 (see Fig. S3). We were not able to isolate this structure ex-situ (Fig. 1(d)), demonstrating the
111 importance of the in-situ scattering measurements. The corresponding GIWAXS pattern in Fig. 1(f) still
112 shows the PbSe {200} and {220} diffraction rings, with no sign of a preferential crystallographic
113 orientation or attachment of the NCs. We conclude that at this stage the NCs behave as hard spheres.
114 Indeed, hard sphere interactions between NCs confined on a 2-D interface leads to entropically driven
115 packing into a hexagonal structure [21,22]. Our difficulty in isolating this phase ex-situ indicates that
116 short-range repulsive contributions from the solvent may be important to the hard sphere-like
117 interaction potential.

118 At longer times, a complete monolayer of NCs is adsorbed at the interface. The NCs form a 2-D
119 pseudo-hexagonal close-packed layer (Fig. 1(g)), with bond-angles deviating from the 60° of a perfect
120 hexagonal structure. In the corresponding ED pattern the {111} and {222} rings are missing, meaning
121 that all NCs have a {100} facet pointing upwards (see Fig. S4). Moreover, the ED pattern shows
122 diffraction arcs rather than full rings, indicating that the NCs have a preferred crystallographic
123 orientation in the 2-D plane. The width of the arcs reflects the remaining in-plane rotational freedom
124 of the NCs. In the GISAXS pattern obtained 30 minutes after the start of the experiment (Fig. 1(i)) the
125 first diffraction rod has moved further from the origin, indicating that the average NC–NC distance
126 has decreased compared to Fig. 1(e). The diffraction peaks are broader than before, consistent with a
127 peak splitting due to deviations of the superlattice symmetry from perfectly hexagonal (see
128 Supplementary Methods 3). An alternative explanation for the broadening of the GISAXS reflections
129 could be the increase of superlattice disorder due to evaporation of residual solvent [23,24].
130 However, we point out that we scooped a sample of this exact sample and confirmed the formation
131 of the square superlattice (see figure S5), supporting the former interpretation of the scattering data.
132 In the corresponding GIWAXS pattern (Fig. 1(j)) we observe the first indications of spots of increased
133 intensity on the atomic diffraction rings, indicative for NC orientation with a $\langle 100 \rangle$ axis perpendicular
134 to the liquid-gas interface. In Fig. 1(h) many NC–NC atomic connections have formed, but not yet all
135 NCs make the maximum number of four NC–NC bonds with their in-plane {100} facets. The diffraction

136 arcs in the ED pattern have further narrowed, since the rotational freedom has decreased with
 137 respect to the pseudo-hexagonal phase of Fig. 1(g).

138 Finally, the NCs attain a square ordered structure (Fig. 1(k,l)) with the $\langle 100 \rangle$ direction pointing
 139 upward and orientational order in the 2-D plane (inset Fig. 1(k)). Furthermore, the NCs attach, as
 140 evidenced not only in the TEM image (Fig. 1(k)), but also from the narrowing of the $\{200\}$ diffraction
 141 spot in the horizontal direction in the GIWAXS pattern (Fig. 1(m)). This is confirmed by later TEM
 142 measurements on the structure formed during the in-situ measurement (Fig. S5).

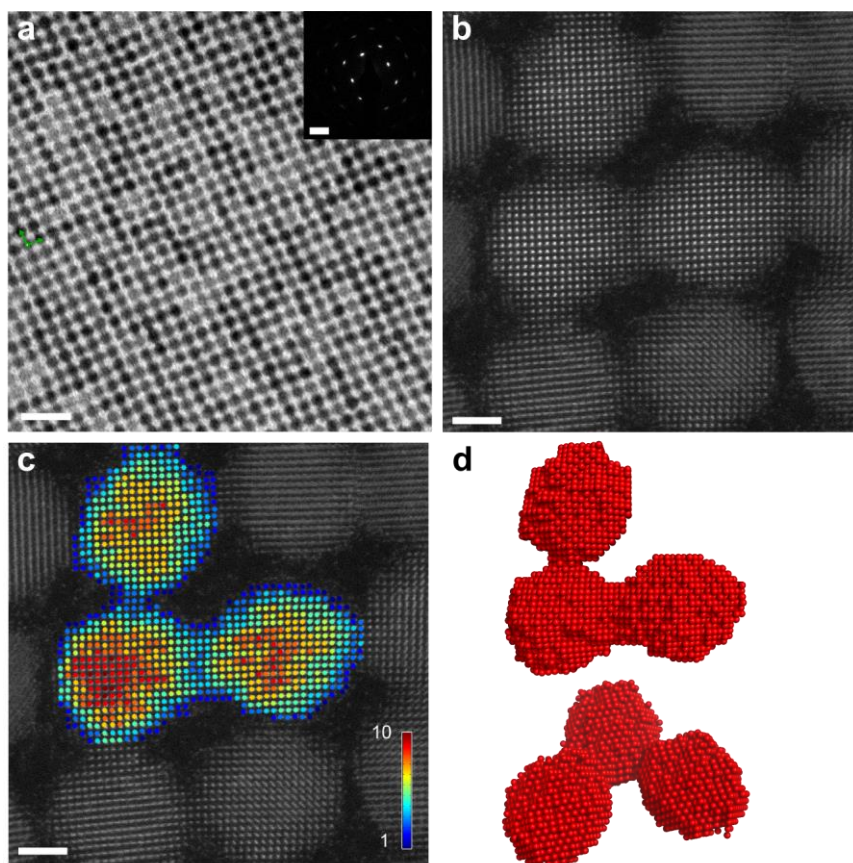


143 **Figure 2: Quantitative analysis of the GISAXS and GIWAXS data.** (a) Fitted peak positions of the first
 144 diffraction rod q_1 in the horizontal scattering direction from the in-situ GISAXS measurements depicted
 145 in Fig. 1. From the position of the diffraction rod the lattice spacing is calculated. (b) Evolution of the
 146 peak width of the in-plane $\{200\}$ atomic reflection in the horizontal scattering direction $q_{||}$ over time as
 147 measured with GIWAXS. The black line is the calculated position of the $\{200\}$ reflection for a rock salt
 148 PbSe crystal structure with a lattice vector of 6 Å.

149 We now investigate in more detail the structural changes observed in the in-situ experiments. We
 150 calculate the time-evolution of the nanoscale lattice spacing from the position of the first diffraction
 151 rod in GISAXS (see Fig. 2(a)). The fitted peak position in reciprocal space (left axis) increases from 0.74
 152 nm⁻¹ to 0.83 nm⁻¹. Realizing that the initial structure has hexagonal symmetry while the final structure
 153 is square, this corresponds to a contraction of the NC-NC distance by 17%, from 9.1 nm after 1200 s
 154 after injection, to 7.6 nm at 2700 s (Fig. S3).

155 The initial NC-NC distance of 9.1 nm is as expected in a hexagonal monolayer of NCs of 5.7 ± 0.6 nm
 156 core diameter separated by oleic acid ligands (roughly 2 nm in length). In the final oriented attached
 157 square structure, however, the NC-NC distance of 7.6 nm is 34% larger than the original PbSe NC core
 158 diameter. This shows that necking takes place during the atomic attachment, i.e. the formation of a
 159 crystal bridge between opposed $\{100\}$ facets [2,5,25].

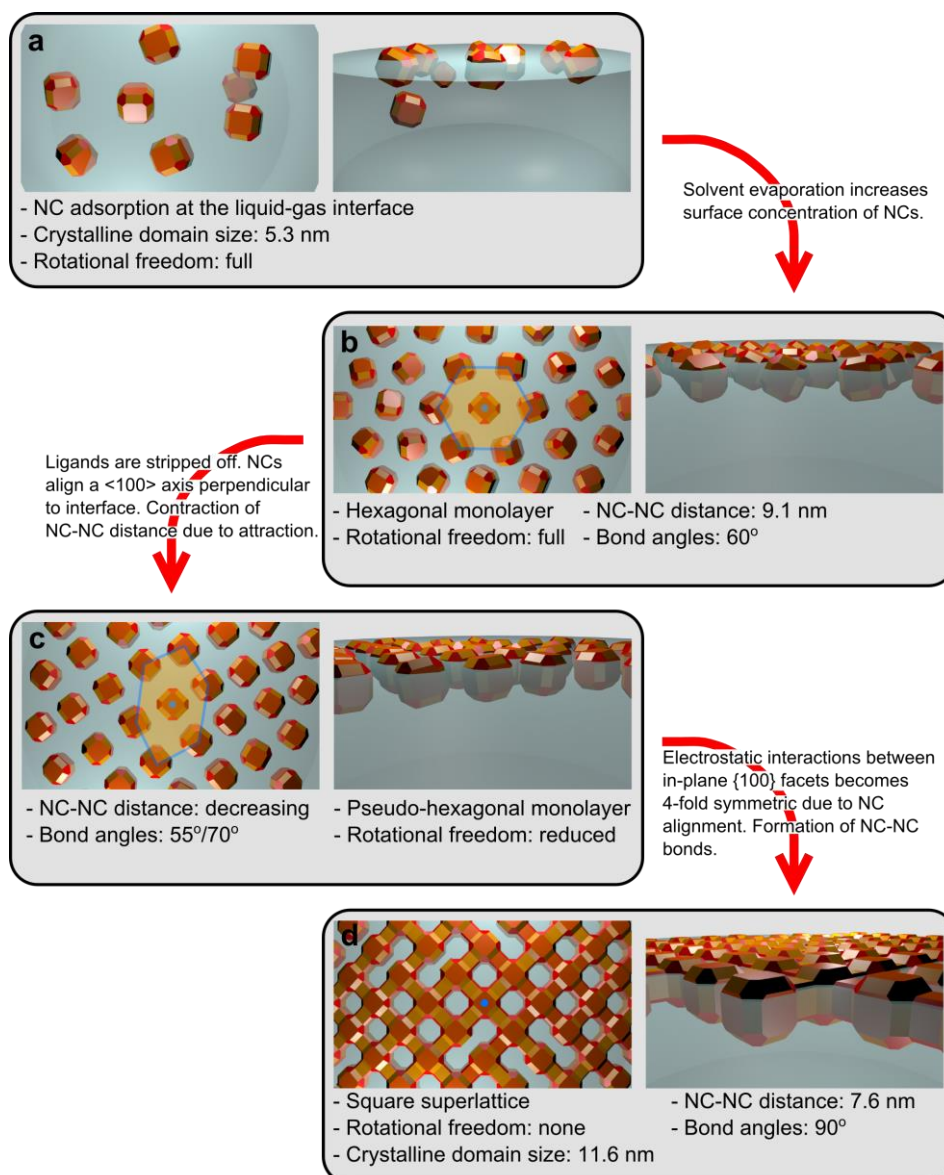
160 The increase of the average atomic coherence length during the formation can be extracted from the
 161 width of the horizontal atomic $\{200\}$ reflections in GIWAXS (see Fig. 2(b)). The FWHM of the $\{200\}$
 162 peak of individual NCs in dispersion equals 1.1 nm^{-1} , corresponding to an average crystalline domain
 163 size of 5.9 nm, consistent with the NC sizes measured with TEM. During the in-situ experiments, the
 164 FWHM decreased to a value of 0.7 nm^{-1} after 31 minutes and 0.5 nm^{-1} after 40 minutes. These values
 165 correspond to crystalline domain sizes of 9.1 nm and 13.2 nm in the horizontal $\langle 100 \rangle$ direction. We
 166 conclude that when NCs attach atomically, the size of single-crystalline domains grows to on average
 167 to a lower limit of two to three NC diameters (see also Fig. S7), which agrees with the TEM sample
 168 obtained from the same experiment (Fig. S5).



169 **Figure 3: HAADF-STEM and atom counting reconstruction on the attached NCs.** (a) Typical overview
 170 bright-field TEM image on a square superlattice. Inset shows the corresponding ED pattern. (b) More
 171 detailed HAADF-STEM image on NCs attached in a square superlattice, showing truly epitaxial
 172 connections and connections with crystal defects. (c) Results from the atom counting procedure, using
 173 (b) as an input image. The colorbar represents the number of detected atoms in the column. (d)
 174 Topview and sideview of the reconstructed atomic model. Scale bars equal 20 nm in **a** (20 nm^{-1} in the
 175 ED inset) and 2 nm in **b** and **c**.

176 In order to study the degree of atomic coherency inside the superlattice, we performed aberration
 177 corrected high angle annular dark field (HAADF) scanning transmission electron microscopy (STEM)
 178 measurements to investigate the atomic lattice. First, Fig. 3a shows an overview of part of a square
 179 sheet, showing that the square nanogeometry is present over many unit cells. In the atomically
 180 resolved image of Fig. 3(b), we observe atomic connections between the nanocrystals that are fully
 181 coherent, and some defective connections as well. These defective connections and the natural
 182 dispersion in the nanocrystal size must affect the perfectness of the square geometry, i.e. lead to
 183 some variation in the translation vectors. In the supplementary information (Fig. S22) we show that
 184 the overall square periodicity (although with its intrinsic variation) is essentially preserved when it is
 185 considered over different length scales. From the HAADF-STEM image we extract the number of
 186 atoms in each projected atomic column using atom counting (Fig. 3(c)). [26,27] These numbers can
 187 then be used as an input for an iterative energy minimization scheme in order to obtain a 3D model
 188 for the investigated superlattice as illustrated in Figures 3(d). [28,29] More experimental details are
 189 provided in the Methods section and an additional example of two connected nanocrystals is
 190 presented in Fig. S23.

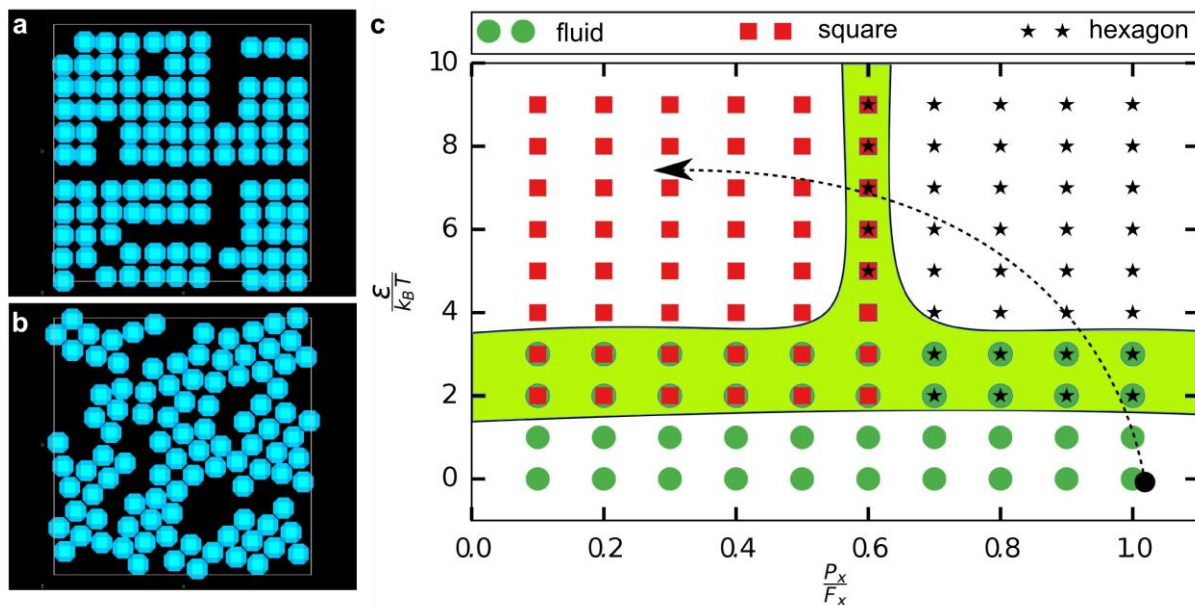
191 Combining all information from the in-situ and ex-situ experiments, we postulate a model for the
 192 reactive self-assembly of PbSe nanocubes into the square oriented attached superlattice.



193 **Figure 4: Schematic mechanism of the consecutive phase transitions during the reactive self-assembly of**
 194 **the PbSe NCs.** Left image shows top views, right image side views. **(a)** As the solvent evaporates, the
 195 concentration of the NCs increases, and the particles adsorb at the liquid-gas interface. **(b)** The central
 196 NC is indicated with a blue dot. The increase in NC concentration forces the particles to form a
 197 hexagonally packed monolayer. **(c)** The ligands on the {100} facets stabilizing the particles in the
 198 toluene slowly dissolve in the ethylene glycol substrate, thus increasing the {100} facet-to-facet
 199 attractive interaction and decreasing the NC-NC distance. Due to the directionality of the in-plane
 200 {100} attractions, the superlattice transforms into a pseudo-hexagonal structure. **(d)** Once the particles
 201 are sufficiently close, they connect atomically via necks; the superlattice obtains a square geometry.

202 Fig. 4 shows cartoons of the different phases occurring in the reactive self-assembly. For clarity we
 203 omitted the oleic acid ligands from the image. During the toluene evaporation the NCs adsorb at the
 204 liquid-gas interface without long-range order (a). As the NC concentration at the interface increases,
 205 they start to form a hexagonally packed monolayer at the interface (b). The NCs still behave similar to
 206 hard spheres, as any anisotropic interaction is screened by the oleate ligands. Possibly, oleate ligands

207 weakly attached to the {100} facets [30], detach and are absorbed in the ethylene glycol phase. The
 208 particles align one of their <100> directions perpendicular to the liquid-gas surface. The rotational
 209 freedom in plane is gradually reduced, in favor of electrostatic and van der Waals interactions
 210 between opposed {100} facets. This also results in a reduced NC–NC distance (c). Due to the
 211 directionality of these in-plane {100} attractions, the superlattice has to change its symmetry from
 212 hexagonal to square. A similar transition between hexagonal and square symmetry has been
 213 predicted from Monte Carlo simulations for a monolayer of hard truncated nanocubes confined at an
 214 interface [31]. Once the NCs are in close proximity, crystalline bridges grow between neighboring NCs
 215 (d). This necking has also been observed in a chemically distinct case of NC attachment [8,32,33].



216 **Figure 5: Monte Carlo simulations on the truncated nanocubes confined to a 2D plane. (a)** Square phase
 217 ($P_x/F_x = 0.1$, $\epsilon/k_B T = 6$) and **(b)** hexagonal/pseudo-hexagonal phase ($P_x/F_x = 0.8$, $\epsilon/k_B T = 6$)
 218 obtained for different sizes of the attractive patches on the {100} facets. **(c)** State diagram for the
 219 truncated cubes with attractive {100} facets as a function of the relative attractive patch size on a
 220 {100} facet P_x/F_x , and the square-well interaction strength $\epsilon/k_B T$ between the attractive patches.
 221 The arrow depicts a possible route that describes the different phases observed in our experiments.
 222 The green shaded area shows regions where multiple phases coexist.

223 To test the postulated model, we investigated the formation of superlattices from PbSe NCs adsorbed
 224 at the liquid-gas interface using Monte Carlo simulations with periodic boundary conditions in the
 225 canonical ensemble, i.e., we fixed the number of particles N , the volume V , and the temperature T of
 226 the system. We model the NCs by truncated cubes as depicted in Fig. S9. The cubes are confined to a
 227 2D plane and are oriented such that the {100} facet points upwards. The nanocrystals are allowed to
 228 move freely in this plane. In the SI we calculate the interaction potential between two nanocrystals,
 229 which is the sum of the electrostatic and London interactions between all the atoms of the
 230 nanocrystals (see Supplementary Methods 7). The ligand-free {100} facets lead to an attractive driving
 231 force that attempts to position the nanocrystals with their vertical {100} facets face-to-face (see Fig.
 232 S24). This directional driving force is mimicked in the simulations by introducing small patches on the
 233 center of the vertical {100} facets. We assume the cantellated cubes to interact as hard particles, but
 234 with the attractive patchy interaction between the {100} facets. The patchy interaction is modelled as
 235 a square patch that interacts with an attractive square-well potential [34,35]. The patch size is defined
 236 by the ratio of the length of the patch P_x and the length of the {100} facet F_x , i.e., P_x/F_x , and the

237 attraction strength is given by $\varepsilon/k_B T$ with k_B Boltzmann's constant. We simulate the self-assembled
238 structures of the NCs as a function of the size of the attractive patch and the attraction strength in
239 order to shed light on the contraction and symmetry change of the hexagonally packed layer towards
240 the square superlattice, as shown in Fig. 1(g) to 1(k) and Fig. 4.

241 In Fig. 5(a) and 5(b), we show two typical configurations of the self-assembled structures for the
242 cantellated cubes with different patch size. We clearly find that the self-assembled structure depends
243 sensitively on the patch size, which determines the directionality of the attractive interaction. For a
244 stronger directionality, i.e. smaller patch size, we observe a square symmetry for the superlattice (see
245 Fig. 5(a)) whereas for a less directional interaction, i.e. a larger patch size, the superlattice shows
246 hexagonal symmetry (see Fig. 5(b)). In Fig. 5(c) we present the state diagram of the nanocrystals as a
247 function of the patch size P_x/E_x , and attraction strength $\varepsilon/k_B T$. We observe that the particles self-
248 assemble into a superlattice for attraction strengths $> 4 k_B T$, even with very small attractive patch
249 sizes. (see also Supplementary Methods 7). The results corroborate our interpretation of the
250 experimental data that the directional electrostatic and van der Waals interactions between the
251 vertical {100} facets drive the phase transition from hexagonal to square NC ordering and keep the
252 {100} facets face-to-face, finally enabling an atomic necking process and growth of attached
253 nanocrystals that form single crystalline domains.

254 The fact that it is possible to monitor in-situ the adsorption of colloidal particles at a liquid surface and
255 to reveal the ensuing structural transformations of the particle monolayer will further our
256 understanding of the mechanisms of interfacial self-assembly processes and the differences with self-
257 assembly in three dimensions. This may result in bottom-up routes towards a diversity of 2-D
258 electronic or photonic materials based on nanocrystals or (anisotropic) polymer-type colloids. We
259 remark that improvements in the atomic coherency are desired for high quality 2-D optoelectronic
260 materials. In such a way, colloid self-assembly can become a feasible alternative for top-down
261 lithography based methods.

262

263 [METHODS]

264 **Nanocrystal synthesis** The PbSe nanocrystals used for the oriented attachment experiments in this
265 study were prepared using the method described by Steckel et al. [36]. The synthesis was performed
266 in a glovebox with a water and oxygen free environment. (a) 4.77g of lead acetate trihydrate
267 (99.999% Aldrich), 10.35g of oleic acid (OA, 90% Aldrich) and 39.75g octadecene (ODE, 90% Aldrich)
268 were heated to 130°C under low pressure (10^{-3} bar) for approximately 4 hours. (b) A second mixture
269 containing 3.52g Se (99.999% Alfa Aesar), 46.59 mL trioctylphosphine (TOP, 90% Fluka) and 0.41mL
270 diphenylphosphine (DPP, 98% Aldrich) was prepared by dissolving the Se. Subsequently solution (a)
271 was heated in a three-necked round-bottom flaks to 180°C after which 15mL of solution (b) was
272 rapidly injected. The particles were grown for approximately 60 seconds, after which the reaction was
273 quenched with 20mL butanol. After the solution was cooled down to approximately 50°C, 10 mL
274 methanol was added to induce precipitation of the nanocrystals. The resulting suspension was
275 centrifuged at 2500 rpm for 10 minutes, the supernatant was removed and the washed particles were
276 redispersed in toluene. This washing procedure was repeated two times.

277 **Oriented attachment of truncated PbSe nanocubes** The ex-situ oriented attachment was performed at
278 20°C inside a glovebox with $<1\text{ppm O}_2$ and $<1\text{ppm H}_2\text{O}$. A glass petri dish (\varnothing 27mm) was filled with 6.5
279 mL ethylene glycol. The nanocrystal (NC) solution with an initial concentration of $3.0 \times 10^{-5} \text{ mol/L}$ was
280 diluted by adding 4 μL of the NC solution to 800 μL of toluene. A total volume of 350 μL of this

281 dispersion was drop cast gently on top of the ethylene glycol. The ethylene glycol serves as an
282 immiscible liquid substrate for the NC solution. After drying the NC solution on top of the EG for 60
283 minutes, a sample was scooped from the ethylene glycol interface on a copper TEM grid and dried in
284 vacuum to remove any residual ethylene glycol.

285 **In-situ GISAXS/WAXS** The in-situ X-ray scattering experiments under grazing incidence were performed
286 at beamline ID10 of the European Synchrotron Radiation Facility (ESRF), Grenoble. The energy of the
287 incident X-ray beam was set at 10.0 keV, below the Pb and Se absorption edges to minimize beam
288 damage. We optimized the grazing angle to 0.3° for the best signal-to-noise ratio on both GIWAXS
289 and GIWAXS detectors. The scattering was recorded by two Pilatus detectors. The GIWAXS patterns
290 were recorded on a Pilatus 300K detector with 619x487 pixels, each $172 \times 172 \mu\text{m}^2$ in size, positioned
291 approximately 25 cm from the sample. The GISAXS patterns were recorded on a Pilatus 300K-W
292 detector with 1475x195 pixels, each $172 \times 172 \mu\text{m}^2$ in size, positioned 0.578 m from the sample. Before
293 drop casting the dispersion of NCs on top of the EG substrate, the x-ray beam was aligned to the
294 surface. After drop casting and every three minutes the alignment was repeated in <10 sec to adjust
295 for solvent evaporation. The oriented attachment was performed in a home-built liquid cell, which
296 can be flushed with argon repeatedly to lower the oxygen and water levels (Fig. S10). A Teflon petri
297 dish (\varnothing 64 mm) was filled with 28 mL of ethylene glycol. To the ethylene glycol we added 10 μL of an
298 OA solution (1% (v/v) OA in ethylene glycol). The cell was then flushed five times with vacuum/argon
299 cycles, and was filled with toluene saturated vapour (argon gas blown through hot toluene). Next, the
300 PbSe NC solution (0.5 mL; 1.9×10^{-6} mol/L) was deposited on top of the liquid substrate. As the PbSe
301 NCs proved to be sensitive to beam damage, we scanned the sample position in between the
302 measurement, back and forth over a distance of 4 mm (in 21 steps) in the direction perpendicular to
303 the incident X-ray beam. In this way, the dose of X-ray photons on each position of the sample was
304 minimized. Each frame was recorded with a 10 s integration time, after which the position of the
305 sample was changed. After each sequence of 21 positions, we returned to the starting position and
306 repeated the procedure.

307 **HAADF-STEM imaging and atom counting** HAADF-STEM imaging is performed using an aberration
308 corrected FEI Titan microscope operated at 300 kV. By modelling images as a superposition of
309 Gaussian functions located at the atomic columns, the volume under each peak can be estimated by
310 fitting this model to the region of interest. These volumes are integrated intensities of electrons and
311 thus correspond to scattering cross-sections. In a subsequent analysis, the distribution of scattering
312 cross-sections of all atomic columns is decomposed into overlapping normal distributions, where the
313 number of normal components is selected using an Integrated Classification Likelihood (ICL) approach
314 [25,26]. Based on the analysis of the image shown in Fig. 3, 10 components have been retrieved
315 illustrating the presence of 1 up to a maximum of 10 atoms in a column. The number of atoms in each
316 projected atomic column is then obtained by assigning the component which generates the
317 experimental scattering cross-section with the highest probability. In this manner, a map reflecting
318 the number of atoms in each column is retrieved as illustrated in Fig. 3b. Based on the counting
319 results, a starting 3-D configuration is obtained by positioning all Pb atoms on a perfect crystal grid
320 symmetrically arranged around a central plane. Next, the potential energy of this configuration is
321 calculated using a Lennard-Jones potential and minimized using an iterative scheme. In each iteration
322 step, one atomic column, selected by a monte-carlo based approach, is shifted over one unit cell and
323 the total energy is again calculated. The previous 3D configuration is replaced by the new one if the
324 total energy is decreased. This procedure is repeated until convergence is reached.

325 [ACKNOWLEDGEMENTS]

326 This research is part of the program “Designing Dirac Carriers in semiconductor honeycomb
327 superlattices (DDC13),” which is supported by the Foundation for Fundamental Research on Matter
328 (FOM), which is part of the Dutch Research Council (NWO). JIG acknowledges funding from the Debye
329 and ESRF Graduate Programs. The authors gratefully acknowledge funding from the Research
330 Foundation Flanders (G.036915 G.037413 and funding of postdoctoral grants to B.G. and A.D.B). S.B.
331 acknowledges the European Research Council, ERC grant N°335078 – Colouratom. The authors
332 gratefully acknowledge dr. Ingmar Swart and dr. Marijn van Huis for fruitful discussions. We
333 acknowledge funding from NWO-CW TOPPUNT “Superficial Superstructures”.

334 The X-ray scattering measurements were performed at the ID10 beamline at ESRF under proposal
335 numbers SC-4125 and SC-3786. The authors thank Giovanni Li Destri and Federico Zontone for their
336 support during the experiments.

337 [AUTHOR CONTRIBUTIONS]

338 JIG, CVO, FTR, JH and JLP performed the in-situ GISAXS/WAXS experiments under supervision of OK
339 and AVP. JIG and CVO analysed the GISAXS/WAXS data. The TEM data was collected by CVO, WHE, JIG
340 and JLP. HAADF-STEM and atomic reconstructions were performed by BG, ADB, SVA and SB. APG and
341 MD performed the Monte Carlo simulations. JIG and CVO wrote the manuscript under supervision of
342 OK, AVP, MD, SB, LDAS and DV. DV supervised the whole project. The manuscript was written through
343 contributions of all authors. All authors have given approval to the final version of the manuscript.

344

345 [COMPETING FINANCIAL INTERESTS]

346 The authors declare no competing financial interests

347

348 [ASSOCIATED CONTENT]

349 Supplementary information is available in the online version of the paper. Reprints and permissions
350 information is available online at www.nature.com/reprints. Correspondence and requests for
351 materials should be addressed to DV.

352

353

354 [REFERENCES]

355 1. Evers, W. H. *et al.* Low-dimensional semiconductor superlattices formed by geometric control
356 over nanocrystal attachment. *Nano Lett.* **13**, 2317–2323 (2013).

357 2. Boneschanscher, M. P. *et al.* Long-range orientation and atomic attachment of nanocrystals in
358 2D honeycomb superlattices. *Science* **344**, 1377-1380 (2014). doi:10.1126/science.1252642

359 3. Pound, G. M. & Mer, V. K. La. Kinetics of Crystalline Nucleus Formation in Supercooled Liquid
360 Tin 1,2. *J. Am. Chem. Soc.* **74**, 2323–2332 (1952).

361 4. LaMer, V. K. & Dinegar, R. H. Theory, Production and Mechanism of Formation of
362 Monodispersed Hydrosols. *J. Am. Chem. Soc.* **72**, 4847–4854 (1950).

363 5. Banfield, J. F. Aggregation-Based Crystal Growth and Microstructure Development in Natural
364 Iron Oxyhydroxide Biomineralization Products. *Science* **289**, 751–754 (2000).

365 6. Pacholski, C., Kornowski, A. & Weller, H. Self-assembly of ZnO: from nanodots to nanorods.
366 *Angew. Chem. Int. Ed. Engl.* **41**, 1188–1191 (2002).

- 367 7. Li, D. *et al.* Direction-specific interactions control crystal growth by oriented attachment. *Science* **336**, 1014–1018 (2012).
368
- 369 8. Schliehe, C. *et al.* Ultrathin PbS sheets by two-dimensional oriented attachment. *Science* **329**,
370 550–553 (2010).
- 371 9. Cho, K.-S., Talapin, D. V., Gaschler, W. & Murray, C. B. Designing PbSe nanowires and nanorings
372 through oriented attachment of nanoparticles. *J. Am. Chem. Soc.* **127**, 7140–7147 (2005).
- 373 10. Kalesaki, E., Evers, W. H., Allan, G., Vanmaekelbergh, D. & Delerue, C. Electronic structure of
374 atomically coherent square semiconductor superlattices with dimensionality below two. *Phys.*
375 *Rev. B* **88**, 115431 (2013).
- 376 11. Kalesaki, E. *et al.* Dirac Cones, Topological Edge States, and Nontrivial Flat Bands in Two-
377 Dimensional Semiconductors with a Honeycomb Nanogeometry. *Phys. Rev. X* **4**, 011010
378 (2014).
- 379 12. Beugeling, W. *et al.* Topological states in multi-orbital HgTe honeycomb lattices. *Nat. Commun.*
380 **6**, 6316 (2015).
- 381 13. Evers, W. H. *et al.* High charge mobility in two-dimensional percolative networks of PbSe
382 quantum dots connected by atomic bonds. *Nat. Commun.* **6**, 8195 (2015).
- 383 14. Whitham, K. *et al.* Charge transport and localization in atomically coherent quantum dot solids.
384 *Nat. Mater.* **15**, 557–563 (2016).
- 385 15. Pietra, F. *et al.* Semiconductor nanorod self-assembly at the liquid/air interface studied by in
386 situ GISAXS and ex situ TEM. *Nano Lett.* **12**, 5515–5523 (2012).
- 387 16. Bian, K. *et al.* Shape-anisotropy driven symmetry transformations in nanocrystal superlattice
388 polymorphs. *ACS Nano* **5**, 2815–2823 (2011).
- 389 17. Li, R., Bian, K., Hanrath, T., Bassett, W. A. & Wang, Z. Decoding the superlattice and interface
390 structure of truncate PbS nanocrystal-assembled supercrystal and associated interaction
391 forces. *J. Am. Chem. Soc.* **136**, 12047–12055 (2014).
- 392 18. Choi, J. J. *et al.* Controlling nanocrystal superlattice symmetry and shape-anisotropic
393 interactions through variable ligand surface coverage. *J. Am. Chem. Soc.* **133**, 3131–3138
394 (2011).
- 395 19. Choi, J. J., Bian, K., Baumgardner, W. J., Smilgies, D.-M. & Hanrath, T. Interface-induced
396 nucleation, orientational alignment and symmetry transformations in nanocube superlattices.
397 *Nano Lett.* **12**, 4791–8 (2012).
- 398 20. Weidman, M. C., Smilgies, D.-M. & Tisdale, W. A. Kinetics of the self-assembly of nanocrystal
399 superlattices measured by real-time in situ X-ray scattering. *Nat. Mater.* **15**, 775–781 (2016).
- 400 21. Evers, W. H. *et al.* Entropy-driven formation of binary semiconductor-nanocrystal
401 superlattices. *Nano Lett.* **10**, 4235–4241 (2010).
- 402 22. Bodnarchuk, M. I., Kovalenko, M. V., Heiss, W. & Talapin, D. V. Energetic and entropic
403 contributions to self-assembly of binary nanocrystal superlattices: temperature as the
404 structure-directing factor. *J. Am. Chem. Soc.* **132**, 11967–11977 (2010).

- 405 23. Hanrath, T., Choi, J. J. & Smilgies, D.-M. Structure/processing relationships of highly ordered
406 lead salt nanocrystal superlattices. *ACS Nano* **3**, 2975–88 (2009).
- 407 24. Narayanan, S., Wang, J. & Lin, X.-M. Dynamical self-assembly of nanocrystal superlattices
408 during colloidal droplet evaporation by in situ small angle x-ray scattering. *Phys. Rev. Lett.* **93**,
409 135503 (2004).
- 410 25. Simon, P. *et al.* Interconnection of nanoparticles within 2D superlattices of PbS/oleic acid thin
411 films. *Adv. Mater.* **26**, 3042–3049 (2014).
- 412 26. Van Aert, S., Batenburg, K. J., Rossell, M. D., Erni, R. & Van Tendeloo, G. Three-dimensional
413 atomic imaging of crystalline nanoparticles. *Nature* **470**, 374–347 (2011).
- 414 27. Van Aert, S. *et al.* Procedure to count atoms with trustworthy single-atom sensitivity. *Phys.*
415 *Rev. B* **87**, 064107 (2013).
- 416 28. Jones, L., MacArthur, K. E., Fauske, V. T., van Helvoort, A. T. J. & Nellist, P. D. Rapid estimation
417 of catalyst nanoparticle morphology and atomic-coordination by high-resolution Z-contrast
418 electron microscopy. *Nano Lett.* **14**, 6336–6341 (2014).
- 419 29. Bals, S. *et al.* Atomic scale dynamics of ultrasmall germanium clusters. *Nat. Commun.* **3**, 897
420 (2012).
- 421 30. Woo, J. Y. *et al.* Ultrastable PbSe Nanocrystal Quantum Dots via in Situ Formation of Atomically
422 Thin Halide Adlayers on PbSe(100). *J. Am. Chem. Soc.* **136**, 8883–8886 (2014).
- 423 31. Thapar, V. *et al.* Entropic self-assembly of freely rotating polyhedral particles confined to a flat
424 interface. *Soft Matter* **11**, 1481–1491 (2015).
- 425 32. Sandeep, C. S. S. *et al.* Epitaxially connected PbSe quantum-dot films: controlled neck
426 formation and optoelectronic properties. *ACS Nano* **8**, 11499–11511 (2014).
- 427 33. Baumgardner, W. J., Whitham, K. & Hanrath, T. Confined-but-connected quantum solids via
428 controlled ligand displacement. *Nano Lett.* **13**, 3225–3231 (2013).
- 429 34. Zhang, H., De Yoreo, J. J. & Banfield, J. F. A Unified Description of Attachment-Based Crystal
430 Growth. *ACS Nano* **8**, 6526,6530 (2014).
- 431 35. Zhang, H. & Banfield, J. F. Energy Calculations Predict Nanoparticle Attachment Orientations
432 and Asymmetric Crystal Formation. *J. Phys. Chem. Lett.* **3**, 2882–2886 (2012).
- 433 36. Steckel, J. S., Yen, B. K. H., Oertel, D. C. & Bawendi, M. G. On the mechanism of lead
434 chalcogenide nanocrystal formation. *J. Am. Chem. Soc.* **128**, 13032–13033 (2006).